Journal of Alloys and Compounds 1085 (2026) 191662

Contents lists available at ScienceDirect

Journal of Alloys and Compounds

journal homepage: www.elsevier.com/locate/jalcom

Direct pulsed-field magnetocaloric dynamics of a single melt-spun Ni–Co–Mn–Ti ribbon

Ali Ghotbi Varzaneh [a], Mariana Ríos [b], Catalina Salazar Mejía [c], Meysam Norouzi-Inallu [d], Gowtham Arivanandhan [a], Bagher Aslibeiki [e,f], Tapati Sarkar [f], Manfred Kohl [a], Tino Gottschall [c], Daniel Salazar [b,*], Jingyuan Xu [a,*]

[a] Institute of Microstructure Technology, Karlsruhe Institute of Technology, Karlsruhe, 76344, Germany
[b] BCMaterials, Basque Center for Materials, Applications and Nanostructures, EHU Science Park, Leioa, 48940, Spain
[c] Dresden High Magnetic Field Laboratory (HLD-EMFL), Helmholtz-Zentrum Dresden-Rossendorf, Dresden, 01328, Germany
[d] Mechanics of Materials Lab, School of Energy Systems, LUT University, Lappeenranta, 53850, Finland
[e] Faculty of Physics, University of Tabriz, Tabriz, Iran
[f] Division of Solid State Physics, Department of Materials Science and Engineering, Uppsala University, SE-751 03, Sweden

ARTICLE INFO

Keywords:
All-*d*-metal Ni–Co–Mn–Ti ribbons
Martensitic transformation
Magnetocaloric effect
Direct adiabatic temperature change
Pulsed magnetic fields
Transformation dynamics

ABSTRACT

The magnetocaloric response of melt-spun all-*d*-metal $Ni_{36}Co_{14}Mn_{37}Ti_{13}$ ribbon samples was investigated with particular emphasis on the direct pulsed-field determination of the adiabatic temperature change, ΔT_{ad}. The ribbons exhibit an A2-like disordered cubic parent phase and a first-order martensitic transformation near room temperature with a thermal hysteresis of about 34 K. Microstructural analysis reveals a dual-grain morphology, which contributes to the broadening of the transformation interval. The maximum isothermal entropy change, ΔS_{iso}, reaches 20.1 J/kg K under 5 T, while the temperature-averaged entropy change (TEC) yields TEC(5) = 17.5 J/kg, indicating promising practical cooling capability. A central result of this work is the direct determination of ΔT_{ad} in melt-spun ribbons with an active mass of only ~1 mg using pulsed magnetic fields up to 20 T. For the direct ΔT_{ad} measurements, a free-standing sample configuration was employed to reduce parasitic heat exchange and better approach quasi-adiabatic conditions. The largest net cooling after a complete field-on/field-off cycle reaches approximately 5 K at 281 K under a 10 T pulse, whereas increasing the field to 20 T does not enhance the overall cooling. Moreover, the temperature decrease evolves with different slopes for different pulse amplitudes, suggesting that both the extent of the field-induced transformation and non-equilibrium transformation dynamics influence the measured response. These results demonstrate the feasibility of direct pulsed-field magnetocaloric measurements on extremely low-mass ribbons and provide insight into their cooling response under high pulsed magnetic fields.

1. Introduction

Magnetic refrigeration based on the magnetocaloric effect (MCE) is considered a promising alternative to conventional vapor-compression cooling because of its potential for higher energy efficiency and reduced environmental impact [1–4]. In particular, materials exhibiting first-order magnetostructural transitions are highly attractive, since the strong coupling between magnetic and structural degrees of freedom can generate large isothermal entropy changes (ΔS_{iso}) and significant adiabatic temperature changes (ΔT_{ad}). However, thermal and magnetic hysteresis, incomplete field-induced transformation, and the resulting irreversibility remain a major challenge for conventional cyclic operation in first-order systems. Therefore, the actual caloric response of such materials should be evaluated under realistic magnetic-field conditions rather than relying solely on indirect thermodynamic estimates.

Among metamagnetic Heusler-type materials, all-*d*-metal Ni–Co–Mn–Ti alloys have recently emerged as particularly promising caloric materials because they combine strong magnetostructural coupling with improved mechanical robustness. In contrast to conventional Ni–Mn–X Heusler alloys containing main-group elements, the predominance of *d*–*d* bonding interactions in these all-*d*-metal compounds is believed to enhance structural stability and mechanical

* Corresponding authors.
E-mail addresses: daniel.salazar@bcmaterials.net (D. Salazar), jingyuan.xu@kit.edu (J. Xu).

https://doi.org/10.1016/j.jallcom.2026.191662
Received 29 June 2026; Received in revised form 21 September 2026; Accepted 9 October 2026
Available online 10 October 2026
0925-8388/© 2026 The Authors. Published by Elsevier B.V. This is an open access article under the CC BY license (http://creativecommons.org/licenses/by/4.0/).
Open access funding enabled and organized by Projekt DEAL.

reliability [5–7]. In addition, these alloys can exhibit large transformation entropy changes, pronounced field-induced martensitic transformations, and multifunctional caloric behavior, including magnetocaloric, elastocaloric, and barocaloric effects [8–11]. Such a combination of functional response and cyclic stability is especially attractive for practical cooling applications and future multi-stimuli operation. Recent studies have further demonstrated that microstructural engineering in Ni–Co–Mn–Ti alloys can significantly improve both cyclic stability and overall functional performance [12].

Besides chemical composition, the processing route and the resulting microstructure play decisive roles in determining the functional response of Ni–Co–Mn–Ti alloys. In particular, rapid solidification into ribbon form provides an effective approach for tailoring grain size, local disorder, crystallographic texture, and internal stress, all of which can strongly influence the martensitic transformation temperature, transformation width, and magnetocaloric performance [13–17]. Moreover, ribbons possess an intrinsically high surface-area-to-volume ratio with reduced thickness, which is advantageous for efficient heat exchange and therefore attractive for compact caloric-device architectures such as multilayer systems and active regenerators [18,19]. Consequently, melt-spun Ni–Co–Mn–Ti ribbons represent a promising materials platform for compact and high-performance caloric cooling technologies.

Despite the growing interest in Ni–Co–Mn–Ti ribbons, their magnetocaloric characterization has so far relied predominantly on indirect approaches based on magnetization or calorimetric measurements [7, 13,15,16,20–24]. This remains a significant limitation for first-order systems, in which hysteresis, dissipation losses, and sweep-rate-dependent transformation kinetics may lead to substantial discrepancies between indirect thermodynamic estimates and the actual adiabatic response [25–27]. In this context, pulsed magnetic fields are particularly valuable because their short duration facilitates quasi-adiabatic conditions, while their high amplitudes enable access to a large fraction of field-induced transformation and provide insight into kinetic effects associated with nucleation and growth [25,26]. Direct measurements of ΔT_{ad} under such conditions are therefore particularly useful for evaluating the actual caloric response of first-order magnetocaloric materials, where hysteresis and transformation dynamics may cause deviations from quasi-equilibrium thermodynamic behavior.

Another important aspect concerns the role of hysteresis. In conventional magnetocaloric cooling cycles, large hysteresis is generally considered detrimental because it reduces reversibility and increases energy losses [26–28]. However, recent studies have suggested that irreversible caloric responses may also be functionally exploited in specifically designed hybrid or hysteresis-assisted cooling concepts, in which a pulsed magnetic field provides rapid cooling while recovery of the initial state is achieved in a subsequent step by conventional refrigeration or an additional external stimulus, such as stress or pressure [26,29,30]. From this perspective, the hysteretic nature of Ni–Co–Mn–Ti alloys should not be regarded solely as a limitation, but also as a potentially useful characteristic for advanced hybrid and multicaloric cooling concepts, provided that the material retains sufficient mechanical integrity.

In this work, melt-spun $Ni_{36}Co_{14}Mn_{37}Ti_{13}$ ribbons are investigated, with emphasis on the interplay between crystal structure, microstructure, martensitic transformation, and magnetocaloric behavior. Particular attention is devoted to the direct determination of ΔT_{ad} under high pulsed magnetic fields, enabling the inverse and conventional caloric contributions, as well as the assessment of hysteresis- and sweep-rate-dependent transformation dynamics in ribbon geometry. Beyond evaluating the magnitude of the caloric response, the present study examines how hysteresis and non-equilibrium transformation behavior influence the realistic cooling response of first-order ribbon systems under pulsed magnetic-field conditions. These results provide direct insight into the realistic caloric response of metamagnetic Ni–Co–Mn–Ti ribbons and help evaluate their potential for compact and high-performance caloric cooling applications.

2. Material synthesis and characterization techniques

Polycrystalline $Ni_{36}Co_{14}Mn_{37}Ti_{13}$ alloy was prepared from high-purity constituent elements (>99.9%) by arc melting under an argon atmosphere. To ensure chemical homogeneity, the ingot was flipped and remelted several times. An additional 2 wt% Mn was added to compensate for Mn evaporation losses during melting. This compensation value was determined empirically from preliminary alloy-preparation trials using the same melting setup, for which an approximately 2 wt% Mn excess resulted in a final composition closest to the nominal stoichiometry. Ribbon samples were subsequently fabricated by melt spinning under an Ar pressure of 10 psi using a quartz nozzle with a diameter of 0.8 mm and a copper wheel surface velocity of 30 m/s. The as-spun ribbons had a width of approximately 1.5–2 mm and a thickness of approximately 30 μm.

The microstructure and local chemical composition were investigated using scanning electron microscopy (SEM, Zeiss Supra 60VP) equipped with an energy-dispersive X-ray spectroscopy (EDS) detector and a Peltier heating/cooling stage operating in the temperature range from 240 K to 363 K. EDS spectra were acquired at an accelerating voltage of 17 kV with an acquisition time of 90 s. Differential scanning calorimetry (DSC) measurements were carried out using a Netzsch DSC 204 Phoenix calorimeter at a heating/cooling rate of 5K/min to determine the characteristic martensitic transformation temperatures and transformation entropy change. Crystal structure analysis was performed by X-ray diffraction (XRD) using a Bruker D8 diffractometer with Cu Kα radiation (λ=1.5418 Å) operated at 30 kV and 20 mA. The diffraction patterns were collected in step mode with an angular step size of 0.03° and a counting time of 2 s per step.

X-ray photoelectron spectroscopy (XPS) measurements were conducted using a PHI QUANTERA II spectrometer equipped with a monochromatic Al Kα source (hν=1486.6 eV); operated at 15 kV and a take-off angle of 45°. The binding-energy scale was calibrated using the C 1 s reference peak to minimize charging-related shifts. To investigate the subsurface chemical states, depth-profile measurements were performed by successive Ar^+ ion sputtering in 6 s intervals up to a total sputtering time of 300 s prior to spectral acquisition.

Magnetization as a function of temperature, $M(T)$, was measured under different magnetic field using a Quantum Design MPMS SQUID magnetometer in order to characterize the magnetic behavior and evaluate the magnetic-field-induced entropy change associated with the magnetocaloric effect. Direct measurements of the adiabatic temperature change, ΔT_{ad}, were performed in pulsed magnetic fields of 5, 10, and 20 T using a home-built setup at the Dresden High Magnetic Field Laboratory (HLD). A more detailed description of the experimental setup can be found elsewhere [26]. The measurements were carried out on a melt-spun ribbon specimen with approximate dimensions of 2 × 7 mm^2 and an active mass of approximately 1 mg. A customized free-standing mounting configuration (see Fig. 1). was employed to minimize parasitic thermal coupling to the sample holder, improve the quasi-adiabatic character of the pulsed-field measurement, and reduce extrinsic mechanical constraints on the ribbon. The latter is particularly important for martensitic alloys, in which external constraints can modify the transformation behavior and shift the transformation temperature. The total duration of each magnetic-field pulse, including both the rising and falling parts, was approximately 100 ms. The temperature response of the ribbon was monitored using a type-T thermocouple with a wire diameter of 25 μm, whose junction was directly attached to the ribbon surface by spot welding. COMSOL simulations suggest that the finite thermal mass of the thermocouple may reduce the measured ΔT_{ad} amplitude by approximately 10% under representative pulsed-field conditions. As discussed by Salazar Mejía et al. [26], the possible contribution of eddy-current heating was examined and found to be negligible, as the sample temperature returned to its initial value after the pulse under reversible conditions.

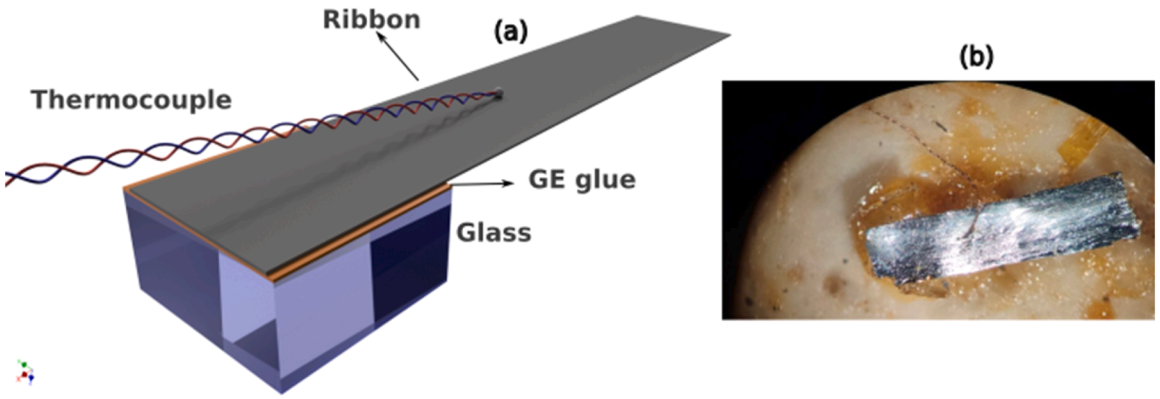


Fig. 1. (a) Schematic illustration of the free-standing ribbon mounting configuration used for the direct magnetocaloric measurements, including the glass support fixed with GE7031 varnish and the welded thermocouple. (b) Actual photo of the mounted ribbon sample.

3. Results and discussion

3.1. Crystal structure, thermal characterization, and microstructure

The room-temperature XRD pattern of the melt-spun ribbon, recorded after heating the sample to 200 °C and subsequently cooling to room temperature, exhibits four main diffraction peaks located at approximately 43.2°, 62.8°, 79.3°, and 94.9°. Structural analysis was performed using Le Bail refinement implemented in the FullProf software (Fig. 2). These reflections can be indexed as (110), (200), (211), and (220) within the smaller bcc indexing scheme used for the profile matching, corresponding to the conventional Heusler-type reflections (220), (400), (422), and (440), respectively [13,22]. The diffraction pattern is well described using a cubic A2 structural model with space group $Im\bar{3}m$, yielding a lattice parameter of $a = 2.956$ Å, which corresponds to approximately 5.912 Å in the equivalent Heusler-type cubic notation. All lattice constants are presented with an approximate accuracy of ±0.005 Å. The Le Bail profile matching yielded $R_p = 75.2\%$, $R_{wp} = 21.4\%$, $R_{exp} = 19.6\%$, and a goodness-of-fit value of $\chi^2 = 1.20$. The relative intensities of the diffraction peaks deviate from those expected for a randomly oriented material, suggesting the presence of preferred crystallographic orientation in the ribbon. Accordingly, a preferred-orientation correction, primarily associated with the (110) reflection, was included in the Le Bail profile matching. However, the present measurement do not allow a quantitative determination of the degree of texture. Since the structure is of the A2 type and exhibits texture, the Rietveld refinement based on XRD data is limited, particularly because all constituent elements have very similar X-ray scattering factors.

A notable feature of the diffraction pattern is the absence of discernible superlattice reflections, particularly those associated with long-range $L2_1$ ordering. This suggests that the parent phase of the ribbon predominantly exhibits a highly disordered cubic structure with A2-like character. Such behavior is consistent with previous studies on all-*d*-metal Ni–Co–Mn–Ti Heusler alloys, where only the fundamental cubic reflections are typically observed, in contrast to conventional Ni–Co–Mn–X systems such as Ni–Co–Mn–In that frequently exhibit additional B2 and/or $L2_1$-related superstructure peaks [31–33]. Nevertheless, distinguishing strictly between A2 and weak B2 ordering in Ni–Co–Mn–Ti alloys using conventional laboratory XRD remains challenging because all constituent elements are 3d transition metals with very similar atomic scattering factors. As discussed by Koch et al. [34], long-range $L2_1$ is generally not stabilized in Ni–Co–Mn–Ti alloys, whereas weak B2-type ordering may still exist, with Ti/Mn preferentially occupying one sublattice and Ni(Co) the other. However, the corresponding superstructure reflections are intrinsically weak and may therefore remain unresolved in conventional XRD measurements. Consequently, although the present refinement supports the predominance of an A2-like parent phase, the presence of weak or partial B2 ordering cannot be completely excluded.

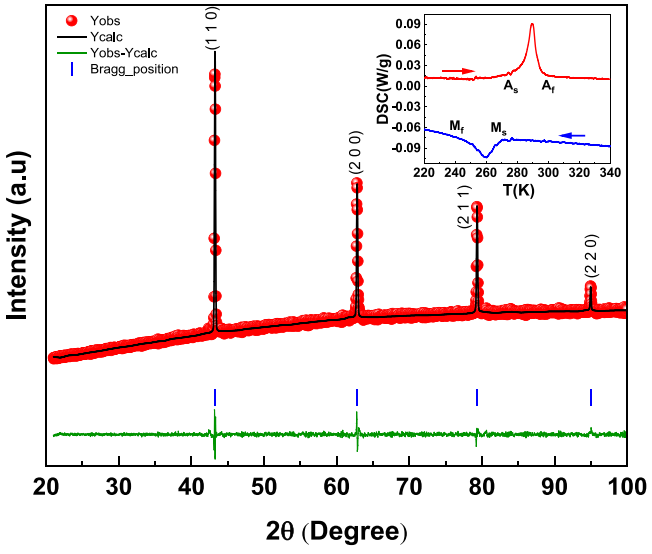


Fig. 2. Room-temperature X-ray diffraction pattern of the ribbon with the corresponding LeBail matching results; the inset presents the DSC heating and cooling curves.

3.1.1. Transformation characteristics

The calorimetric behavior of the ribbon was investigated by DSC at a heating/cooling rate of 5 K/min. As shown in the inset of Fig. 2, the heating and cooling curves exhibit distinct endothermic and exothermic peaks corresponding to the reverse and forward martensitic transformations, respectively. The characteristic transformation temperatures, namely the martensite start (M_s), martensite finish (M_f), austenite start (A_s), and austenite finish (A_f), were determined using the tangent-intersection method and are summarized in Table 1. The transformation

Table 1
Characteristic martensitic transformation temperatures, thermal hysteresis width (ΔT_{hys}) determined from the DSC data and the *M(T)* curve measured under an applied field of 0.005 T, transformation entropy change derived from DSC (ΔS_{DSC}), and entropy change estimated from the Clausius–Clapeyron relation at 5 T ($\Delta S_{C\text{-}C}$).

	M_s (K)	M_f (K)	A_s (K)	A_f (K)	ΔT_{hys} (K)	ΔS (J/kgK)
DSC	273.2	249.0	284.2	293.3	30	ΔS_{DSC}= 24.5
Magnetization	267	250	287	296	34	$\Delta S_{C\text{-}C}$ = 26

entropy change was estimated from the DSC data according to: $\Delta S_{DSC} = \Delta H/T_0$, where ΔH is the transformation enthalpy obtained from the integrated area of the DSC peak and $T_0 = (A_s + A_f)/2$ is the average transformation temperature [35]. The well-defined calorimetric peaks together with the finite thermal hysteresis confirm the first-order nature of the martensitic transformation.

3.1.2. Microstructure and chemical homogeneity

SEM observations reveal that the melt-spun ribbon consists of two distinct grain populations, referred here as small and large grains, as shown in Fig. 3. Higher-magnification micrographs indicate that the small grains have an average size of approximately 1.7±0.6 μm, whereas the large grains exhibit an average size of approximately 4.0±1.3 μm. EDS analyses indicate that both grain populations remain compositionally close to the nominal alloy composition within the experimental uncertainty (<0.7 at%), as illustrated in the radar plot in Fig. 3(e). This suggests that both regions belong predominantly to the same matrix phase with only minor local compositional variations. A characteristic columnar grain morphology is clearly observed across the ribbon thickness (Fig. 3(d)), where elongated grains grow nearly perpendicular to the ribbon surfaces along the thermal gradient established during rapid solidification. This morphology reflects the strong cooling effect of the copper wheel and is characteristic of melt-spun ribbons [14–16].

To further clarify the phase behavior of the two grain populations, *in-situ* temperature-dependent microscopic observations were performed between 240 and 363 K (Fig. 4(a-f)). In the large grains, well-defined martensite variants are clearly visible at 240 K. Upon heating to 303 K, these contrast features disappear almost completely, indicating completion of the reverse martensitic transformation into the austenitic phase. Further heating to 363 K produces no additional visible microstructural changes. In contrast, the small-grain regions show little detectable contrast evolution throughout the investigated temperature range. Therefore, their transformation behavior cannot be directly determined from the present SEM observations. The absence of visible contrast may be related to differences in crystallographic orientation or imaging contrast, while local compositional and microstructural variations may also influence their transformation behavior. Minor compositional variations detected by EDS, including a slightly higher Ti content in the small-grain regions, may contribute to local variations in the transformation behavior [17]. Such microstructural and compositional heterogeneity may also contribute to the relatively broad DSC transformation interval.

Elemental mapping further confirms a relatively homogeneous distribution of Ni, Co, Mn, and Ti throughout the ribbon without evidence of secondary-phase precipitation, as shown in Fig. 5. Moreover, EDS line-scan measurements performed across regions containing both grain populations and their interfaces do not reveal significant compositional segregation. Therefore, the different transformation behavior observed for the two grain populations is more reasonably associated with slight local compositional fluctuations and microstructural effects rather than the formation of secondary phases.

To further investigate the surface chemistry and depth-dependent chemical states of the melt-spun ribbon, XPS depth-profile measurements were performed after successive Ar^+ ion sputtering steps. High-resolution spectra were acquired after each sputtering interval, while survey spectra were recorded every 60 s up to a total sputtering time of 300 s. The corresponding spectra are presented in Fig. 6(a). Distinct signals associated with Ni 2p, Co 2p, Mn 2p, Ti 2p, and O 1 s are clearly observed [19,36].

In addition to the core-level spectra, the valence-band region provides further insight into the electronic structure of the ribbon (Fig. 6 (b)). Two oxygen-related features were observed at the initial surface, namely a contribution near ~5 eV associated with O 2p-derived states and a broader feature around ~22 eV corresponding to O 2 s states. Both signals decrease significantly with increasing sputtering time, confirming their origin from the native surface oxide layer. In contrast, the intense broad band close to the Fermi level remains clearly visible after sputtering and therefore reflects the intrinsic electronic structure of the alloy. As shown by the deconvolution in the inset Fig. 6(b), this low-binding-energy region can be described by two main components centered at approximately 0.4 and 1.6 eV, together with the oxygen-related contribution near 5 eV. Although a strict element-specific assignment is difficult because of the strong overlap between transition-metal electronic states, the component near ~0.4 eV is mainly associated with hybridized Ti 3d and Co 3d states close to the Fermi level, with additional contribution from Ni 3d states. The broader component centered near ~1.6 eV is attributed primarily to the main hybridized Ni/Co/Mn 3d-derived band. The broad and merged character of these low-binding-energy features indicates pronounced d–d hybridization within the all-d-metal Ni–Co–Mn–Ti alloy. Such strong *d–d* hybridization has previously been suggested as one of the key factors contributing to the improved mechanical robustness of Ni–Co–Mn–Ti alloys compared with conventional Ni–Mn–X (X = Sn, Ga, In) Heusler alloys [5–7].

The O 1 s intensity decreases significantly with increasing sputtering time, indicating that the oxygen-containing species are mainly confined to the outermost surface region. This behavior suggests the presence of only a thin native oxide layer, while the subsurface region remains predominantly metallic. The high-resolution Ni 2p spectra exhibits the characteristic metallic Ni doublet, with the main Ni $2p_{3/2}$ and Ni $2p_{1/2}$ peaks located near 852.6 and 870.0 eV, respectively (Fig. 6(c)). The intensity of these metallic peaks progressively increases with sputtering time, whereas oxide-related satellite features remain weak [19,37]. A similar trend is observed for the Co 2p spectra (Fig. 6(d)), where the metallic Co $2p_{3/2}$ and $Co2p_{1/2}$ peaks located at approximately 777.9 and 793.2 eV become increasingly pronounced after Ar^+ sputtering, indicating that Ni and Co remain predominantly in metallic or alloyed states with only limited surface oxidation.

Although all constituent elements are transition metals, Mn and Ti have a stronger affinity toward oxygen than Ni and Co, resulting in more pronounced surface oxidation of these elements. Mn and Ti exhibit more pronounced chemical-state evolution during sputtering. The Mn 2p spectra (Fig. 6(e)) initially show components near 641–642 eV and 652–653 eV, corresponding to oxidized Mn species at the surface. With increasing sputtering time, the spectra shift toward lower binding energies, and the metallic Mn contribution becomes dominant. A similar

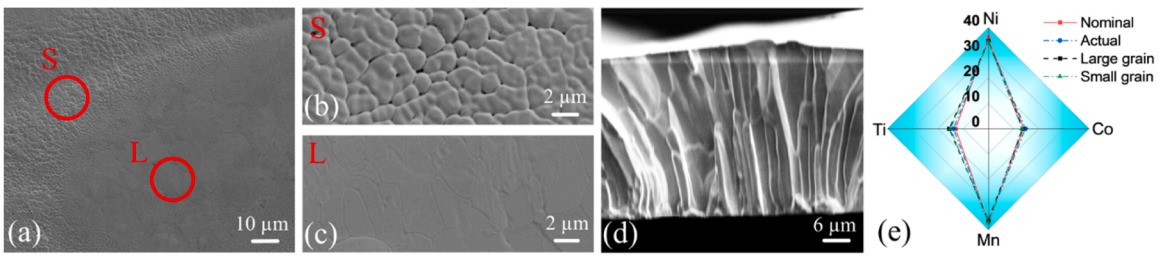


Fig. 3. SEM images of the melt-spun ribbon: **(a)** surface morphology showing small (S) and large (L) grains; **(b, c)** enlarged views of the two regions; **(d)** cross section image of ribbon; **(e)** EDS compositional comparison with the nominal composition.

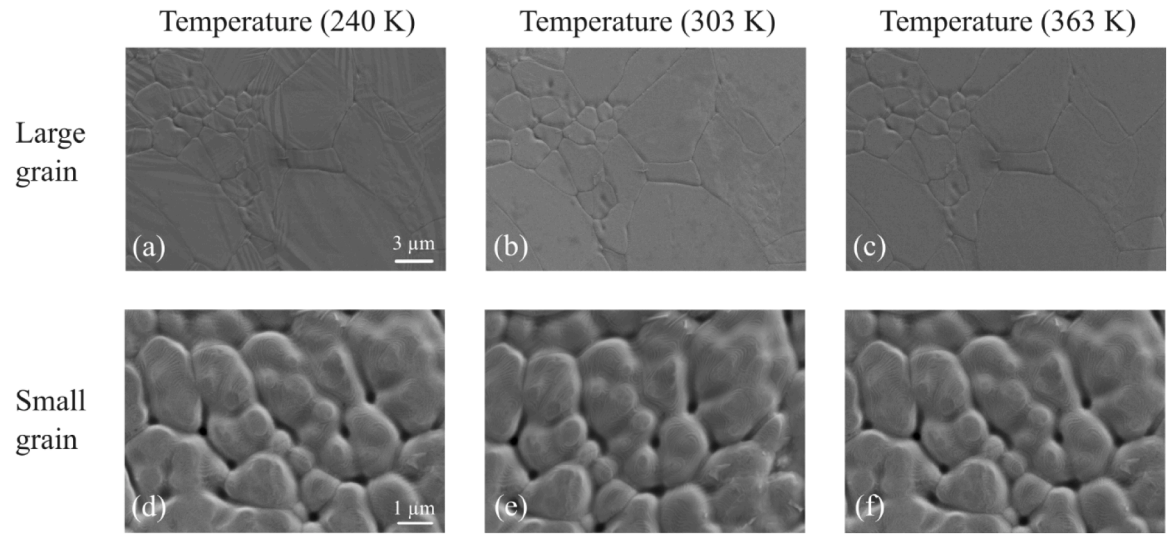


Fig. 4. Temperature-dependent SEM images of representative large-grain and small-grain regions of the melt-spun ribbon. (a–c) Large grain recorded at 240, 303, and 363 K, respectively. (d–f) Corresponding small-grain region imaged at the same temperatures as large grains.

evolution is observed for Ti 2p (Fig. 6(f)), where the spectra gradually evolve from oxide-related features toward metallic/alloyed Ti peaks located near 454.4 and 460.0 eV for the Ti $2p_{3/2}$ and Ti $2p_{1/2}$ components, respectively. The slightly elevated binding energies compared with pure metallic Ti may reflect electronic interactions between Ti and neighboring transition-metal atoms within the alloy lattice. Although the binding-energy scale was calibrated using the C 1 s reference peak to minimize charging-related shifts, Ar^+ sputtering may still induce partial reduction, preferential sputtering, and small binding-energy changes; therefore, a contribution from sputtering-induced effects cannot be completely excluded.

Overall, the XPS depth-profile results are consistent with the presence of a thin native oxide layer at the ribbon surface, whereas the interior of the ribbon remains chemically metallic and relatively oxide-free. The progressive decrease of the O 1 s intensity together with the increasing metallic contributions of the constituent elements with sputtering indicates gradual exposure of the underlying metallic alloy, although partial reduction and preferential sputtering induced by Ar^+ bombardment may also contribute to the observed spectral evolution. These observations are consistent with the good chemical homogeneity revealed by the SEM-EDS analysis.

3.2. Magnetic properties

Fig. 7 presents the temperature-dependent magnetization curves, M (T), measured under different applied magnetic fields. The ribbon exhibits a clear first-order magneto-structural transition accompanied by pronounced thermal hysteresis between the cooling and heating branches. The characteristic transformation temperatures extracted from the M(T) curve measured under 0.005 T using the tangent-intersection method are summarized in Table 1.

With increasing magnetic field, the martensitic transformation shifts toward lower temperatures, indicating stabilization of the ferromagnetic austenitic phase relative to the weak-magnetic martensitic state. From the linear dependence of A_s on magnetic field shown in the inset of Fig. 7, the field sensitivity of the transformation is estimated to be approximately: $dA_s/\mu_0 dH \approx$–3 K/T. The magnetization difference across the transformation, defined as the difference between the magnetization values near A_s and A_f under 1 T, reaches $\Delta M \approx 61$ emu/g. Such a relatively large ΔM reflects strong magneto-structural coupling and is consistent with the considerable magnetic contrast between the ferromagnetic austenite and weak-magnetic martensite. The pronounced field sensitivity is additionally facilitated by the sufficiently large separation between the martensitic transformation and the Curie temperature of the austenite phase, which preserves a high magnetization of the austenitic state during transformation [6]. Although a large ΔM generally favors stronger field-induced transformation and enhanced magnetocaloric response, its role in inverse magnetocaloric Heusler alloys is inherently dual in nature [28,38].

The transformation interval, defined by A_f-A_s, is approximately 13 K. The relatively broad transformation range can be attributed to the heterogeneous ribbon microstructure. In particular, variations in grain size together with A2/B2-related structural disorder are expected to generate local variations in the martensitic transformation temperature, thereby broadening the overall transformation interval [28,39].

Using the Clausius–Clapeyron relation for field-induced martensitic transformation, $\Delta S_{C-C} = -\Delta M/(dT_t/\mu_0 dH)$, the transformation entropy change is estimated to be approximately 26 J/kg K [19,27]. This value is consistent with typical Ni–Co–Mn–Ti metamagnetic alloys and confirms the sizable magnetostructural coupling present in the ribbon. The achievable entropy change is governed by the interplay between ΔM and the field dependence of the transformation temperature. While a larger transformation shift under magnetic field generally promotes a higher fraction of field-induced austenite and therefore a larger structural entropy contribution, it is often accompanied by an increased magnetic entropy contribution. Consequently, optimal magnetocaloric performance is achieved only when an appropriate balance between these competing contributions is realized.

The thermal hysteresis width, ΔT_{hys}, determined from the peak positions of the derivatives of the heating and cooling branches measured under 0.005 T, is approximately 34 K. In all-*d*-metal Ni–Co–Mn–Ti alloys, such large hysteresis is generally associated with the dissipative nature of the first-order transformation and is strongly influenced by stoichiometric homogeneity, atomic disorder, internal stress, quenched defects, and microstructural heterogeneity introduced during rapid solidification [19,38]. The isothermal $M(H)$ curves in Fig. 7(b) also show pronounced magnetic hysteresis in the transformation region. The corresponding hysteresis loss, determined from the area enclosed by the field-increasing and field-decreasing branches, reaches its maximum near 280 K. From the perspective of conventional cyclic magnetocaloric cooling, large hysteresis is usually disadvantageous because it reduces reversibility and increases energy dissipation. However, pronounced hysteresis may also be functionally beneficial in specifically designed hybrid or multicaloric cooling concepts. In such approaches, the field-induced austenitic state can remain stabilized after field removal, while recovery of the initial martensitic state is achieved subsequently

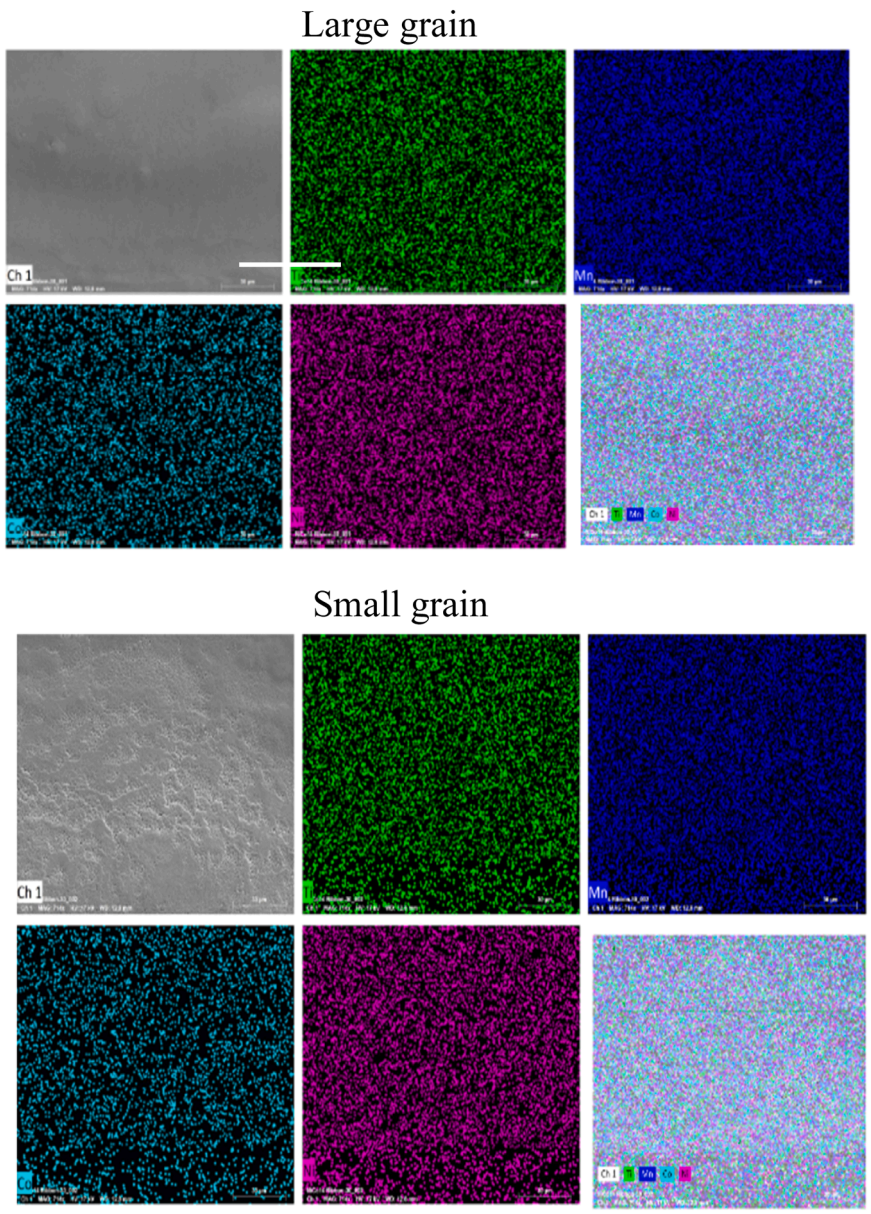


Fig. 5. SEM image and corresponding EDS elemental maps of the large-grain and small-grain regions.

by an additional external stimulus such as stress or pressure [6,29]. Therefore, the large hysteresis observed in the present ribbon should not be viewed solely as a limitation, but also as a potentially useful characteristic for hysteresis-assisted cooling strategies.

3.3. Magnetocaloric effect

The magnetic-field-induced isothermal entropy change, ΔS_{iso}, was evaluated from the from the heating branches of the thermomagnetic *M (T)* curves measured under different constant magnetic fields within the martensitic transformation temperature region using a numerical approximation of the Maxwell relation [40,41]:

$$\Delta S_{iso}\left(T_j, \Delta H\right) = \sum_{i=1}^{n-1} \frac{1}{2}\left(\left(\frac{\partial M_i}{\partial T_j}\right)_{H_i} + \left(\frac{\partial M_{i+1}}{\partial T_j}\right)_{H_{i+1}}\right)\Delta H \quad (1)$$

where $\left(\frac{\partial M_i}{\partial T_j}\right)_{H_i}$ represents the temperature derivative of magnetization under a constant magnetic field. The resulting three-dimensional ΔS_{iso} (T, H) contour map for magnetic fields up to 5 T is shown in Fig. 8. The positive sign of ΔS_{iso} confirms the inverse magnetocaloric effect, indicating that the lattice entropy contribution associated with the field-induced martensite-to-austenite transformation dominates over the opposing magnetic entropy contribution [42,43]. The maximum entropy change reaches approximately 20.1 J/kgK under a magnetic-field change of 5 T near 283 K.

The obtained ΔS_{iso} values are in good agreement with those estimated from both the Clausius–Clapeyron relation and the DSC measurements, confirming the reliability of the calculated entropy change and indicating the absence of artificial spikes commonly associated with first-order transitions. The results further demonstrate that the processing route and resulting microstructure strongly influence the magnetocaloric response. In melt-spun ribbons, rapid solidification introduces grain refinement, local disorder, residual stress, and quenched defects, all of which can modify the martensitic transformation pathway and influence the fraction of field-induced austenite [19]. Nevertheless, despite these intrinsic microstructural effects, the present ribbon exhibits a pronounced entropy change, highlighting the

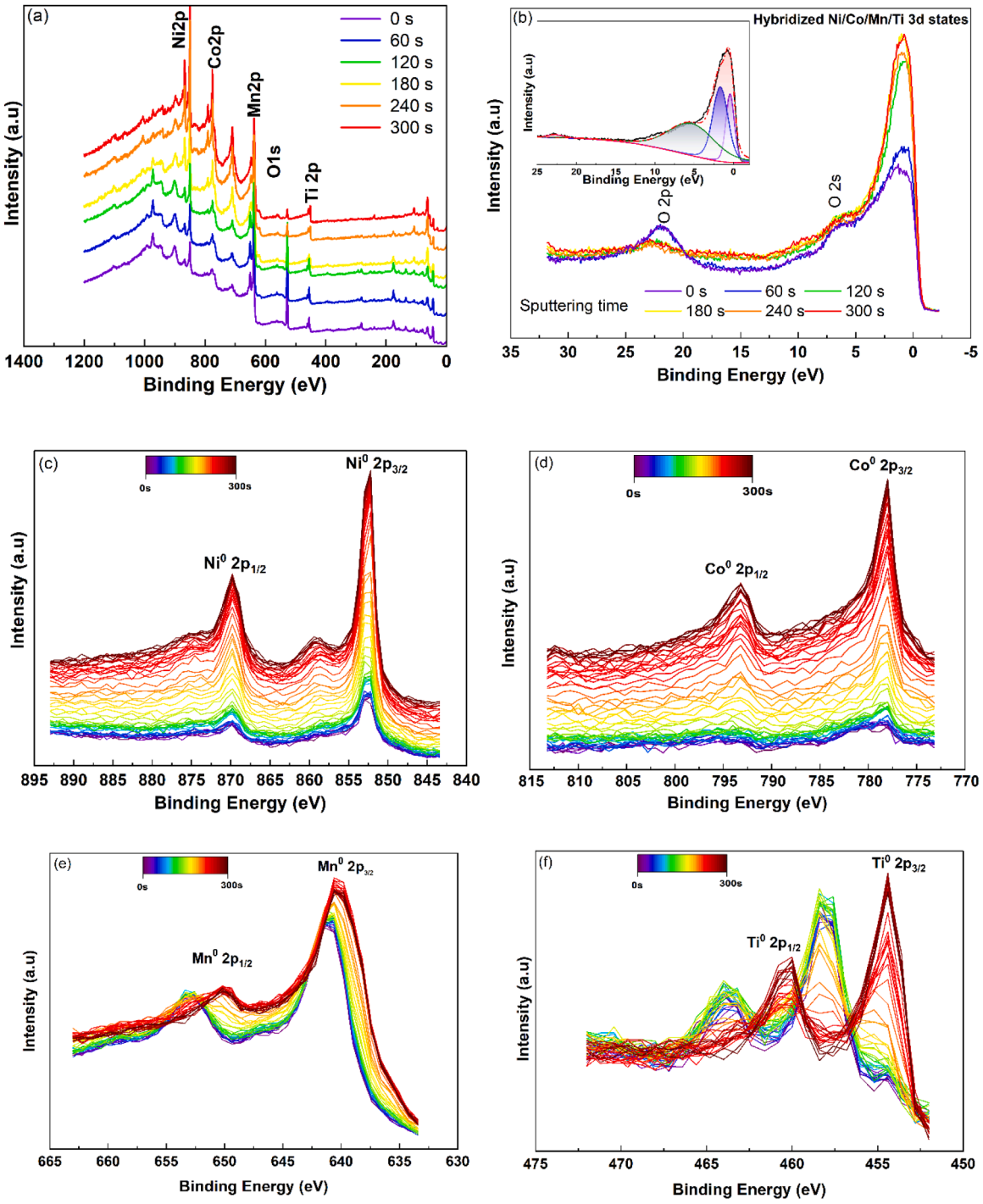


Fig. 6. Survey and high-resolution XPS spectra of ribbon. (a) Survey spectrum confirming the presence of Ni, Co, Mn, and Ti. (b) Valence-band spectra; the inset shows the deconvolution into hybridized transition-metal 3d states and an oxygen-related contribution. (c–f) show core-level spectra of elements with features corresponding to metallic and oxidized states.

strong magnetocaloric potential of melt-spun all-d-metal Ni–Co–Mn–Ti alloys.

In addition to ΔS_{iso}, the temperature-averaged entropy change (TEC) was evaluated as an additional figure of merit for assessing the practical cooling capability of the present ribbon. As proposed by Griffith et al. [44]. TEC is defined as follows:

$$TEC(\Delta T_{lift}) = \frac{1}{\Delta T_{lift}} \left\{ \int_{T_{mid}-\frac{\Delta T_{lift}}{2}}^{T_{mid}+\frac{\Delta T_{lift}}{2}} \Delta S_{iso}(T)_{\Delta H} dT \right\}$$

where ΔT_{lift} represents a temperature range, and T_{mid} is the central temperature at which the TEC (ΔT_{lift}) reaches the maximum value. TEC provides a more application-oriented measure of the useful entropy change within a prescribed temperature lift than conventional width-based criteria. For the present $Ni_{36}Co_{14}Mn_{37}Ti_{13}$ ribbons, the calculated values are TEC(3) = 11.5 J/kg K under $\mu_0\Delta H$ = 2 T, TEC(5) = 17.5 J/kg K and TEC(10) = 16.4 J/kg K under $\mu_0\Delta H$ = 5 T. These values indicate that the ribbon maintains a relatively large effective entropy change over practically relevant operating intervals. A comparison with representative literature data for Ni–Mn–X and closely

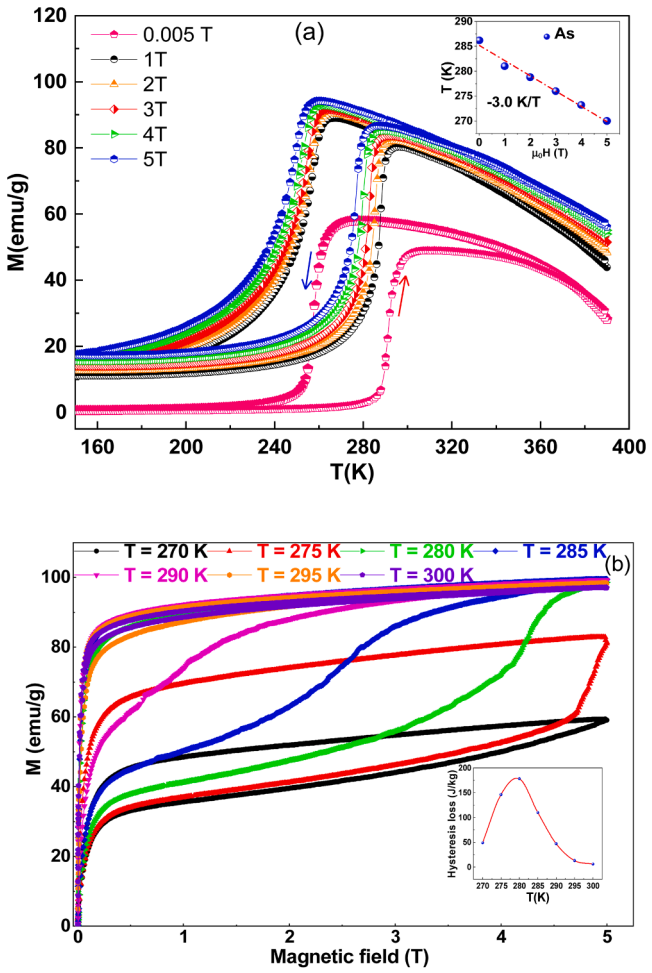


Fig. 7. **(a)** Magnetization curves for the $Ni_{36}Co_{14}Mn_{37}Ti_{13}$ ribbon measured in different applied magnetic fields up to 5 T, on cooling and heating. The inset depicts the A_s vs. magnetic field dependence and related slope of linear approximations in K/T. **(b)** Isothermal $M(H)$curves measured between 270 and 300 K. The inset shows the corresponding hysteresis loss as a function of temperature.

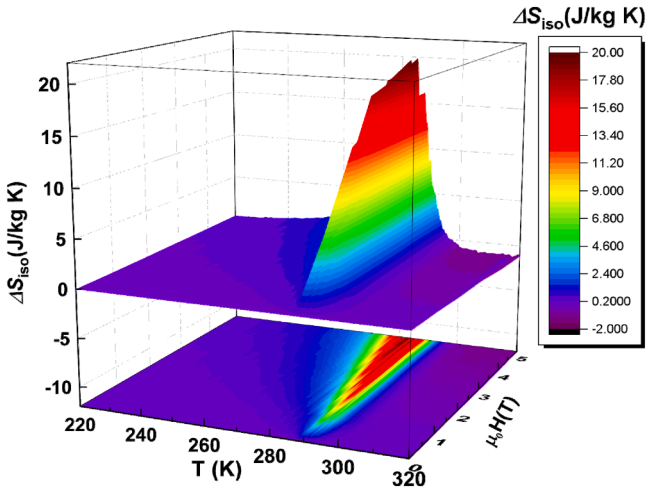


Fig. 8. Three-dimensional contour maps showing ΔS_{iso} as a function of temperature and magnetic field for $Ni_{36}Co_{14}Mn_{37}Ti_{13}$ ribbon.

related all-d-metal Ni–Co–Mn–Ti Heusler alloys further highlights the strong performance of the present ribbons. In particular, the obtained TEC values are higher than many of the reported values for Ni–Mn–X and all-d-metal Ni–Co–Mn–Ti systems and place the present material within the upper-performance range of TEC-based magnetocaloric metrics [45–49].

While the TEC parameter describes the useful entropy change over a given temperature span, it does not account for irreversible magnetic hysteresis losses. Therefore, the influence of hysteresis on the cooling performance was further evaluated using the isothermal $M(H)$ loops shown in Fig. 7(b). The average hysteresis loss over the full-width-at-half-maximum temperature interval of the to ΔS_{iso} (T) curve is approximately 141 J/kg. The refrigerant capacity (RC) at 5 T is approximately 270 J/kg. After accounting for the hysteresis loss, the effective refrigerant capacity, $RC_{\mathrm{eff}} = RC - \langle HL \rangle$, decreases to approximately 129 J/kg, highlighting the significant influence of hysteresis on conventional cyclic magnetic refrigeration.

Fig. 9(a) presents the time dependence of the adiabatic temperature change, ΔT_{ad}, measured under a 5 T pulsed magnetic field at different initial temperatures spanning the martensitic and austenitic regions. For measurements performed within the martensitic state, the sample was thermally reset before each pulse by cooling to 180 K and subsequently heating to the selected target temperature. Owing to the pronounced thermal hysteresis, the measured ΔT_{ad} depends on the thermal history and the corresponding transformation path of the sample. Therefore, the first-pulse ΔT_{ad} reported here should be regarded as a history-dependent

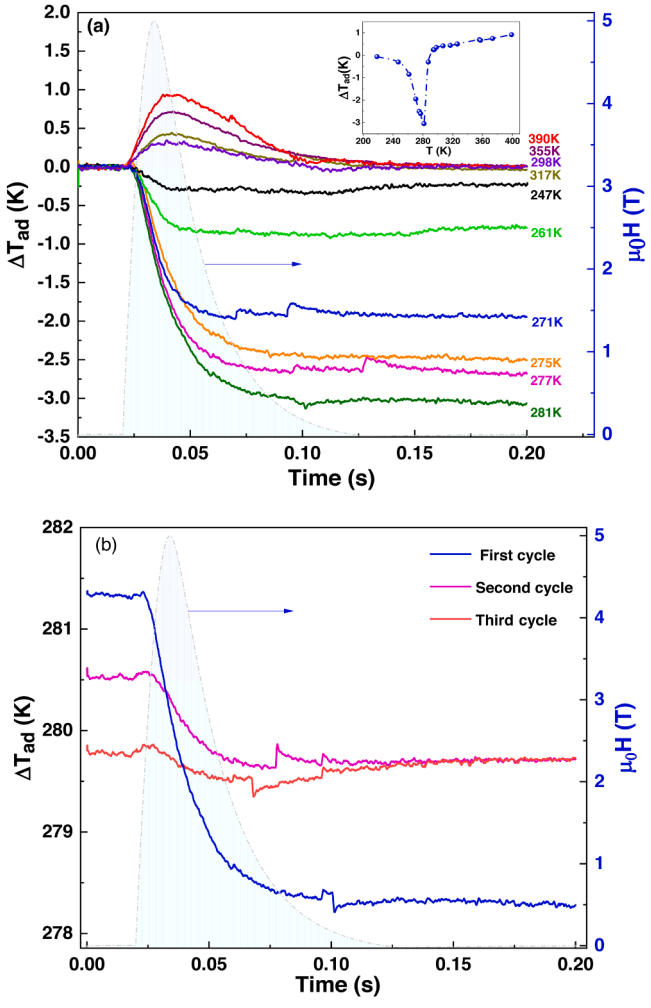


Fig. 9. **(a)** Adiabatic temperature change, ΔT_{ad}, of the ribbon measured directly in a 5 T pulsed magnetic field at different initial temperatures, the blue shaded area represents the magnetic-field pulse profile vs. time and the inset shows ΔT_{ad} as a function of temperature. **(b)** cyclic behavior for 3 cycles.

single-shot response rather than as the fully reversible ΔT_{ad} obtainable during conventional magnetic-field cycling. In the fully austenitic state (for T $\geq$ 298 K), a positive ΔT_{ad} is observed, consistent with the expected conventional magnetocaloric response. Notably, the maximum of the positive temperature signal does not coincide with the magnetic-field maximum but instead appears with a delay of approximately 9 ms. [26]. In the fully magnetic-transition region, this offset is mainly related to the finite thermal response of the thermocouple, the non-instantaneous thermal coupling between the sample and the sensor, and the non-negligible thermal mass of the thermocouple relative to the very small sample mass. In contrast, in the first-order transformation region, the much larger delay between the field maximum and the extremum of the measured ΔT_{ad} signal suggests that, in addition to the sensor response, the intrinsic dynamics and hysteretic character of the martensitic transformation also play a role. Because these contributions cannot be rigorously separated, the maximum temperature decrease after the complete field-on/field-off process was taken as the relevant experimental quantity, and its evolution is shown in the inset of Fig. 9 (a).

Within the martensitic transformation region, the alloy exhibits the expected inverse magnetocaloric behavior, i.e., the sample cools upon application of the magnetic field. Although the reduction of magnetic entropy associated with field-induced spin alignment contributes with the opposite sign, the endothermic reverse martensitic transformation clearly dominates the overall response. Consequently, for temperatures below approximately 280 K, ΔT_{ad} becomes negative and its magnitude increases upon approaching A_s. At 281 K, the maximum observed temperature decreases after the complete field-on/field-off process is about 3 K. Importantly, the cooling does not stop at the field maximum, but continues during the down-sweep of the magnetic pulse. Based on the conventional magnetocaloric response measured at higher temperatures, the contribution expected from field-induced austenite in this temperature range should remain small, i.e. below about 0.2 K for 5 T, and therefore cannot by itself account for the continued temperature decrease during field removal. Thus, as discussed above, the apparent plateau in the measured response within the martensitic region reflects the combined influence of sensor-related effects and the intrinsic dynamics of the martensitic transformation [25,27]. Importantly, while these effects complicate the interpretation of the transient signal during the pulse, they do not prevent a reliable determination of the post-pulse net cooling, since the measured temperature rapidly approaches a stable level after the field has been removed.

For the consecutive-pulse measurements in Fig. 9(b), carried out near 281 K, the sample was kept at zero magnetic field for approximately 1 min between successive pulses to allow thermal stabilization; however, no full thermal reset was performed. The second pulse was applied at a slightly lower initial temperature than the first, while the third pulse started from approximately the final temperature reached after the second pulse. Possible isothermal relaxation and thermal minor-loop effects may influence the phase state during the waiting periods. Although the martensite/austenite fractions cannot be quantified from the present measurements, the strongly reduced response of the second pulse and the nearly absent response of the third pulse are consistent with incomplete recovery of the initial martensitic state, suggesting that a significant fraction of the field-induced austenite is retained between successive pulses. Overall, the repeated-pulse data demonstrate a strong history dependence and with the large thermal hysteresis. Although such behavior limits fully reversible single-stimulus magnetocaloric cycling, it may still be exploited in hybrid or hysteresis-assisted multicaloric cooling concepts [6,42], where an additional external stimulus such as stress or pressure is used to restore the initial thermodynamic state.

Fig. 10 (a) compares the time-dependent adiabatic temperature change measured at 281 K under pulsed magnetic fields of 5, 10, and 20 T. The largest net cooling after the complete field-on/field-off process is obtained under the 10 T pulse, reaching approximately 5 K, whereas

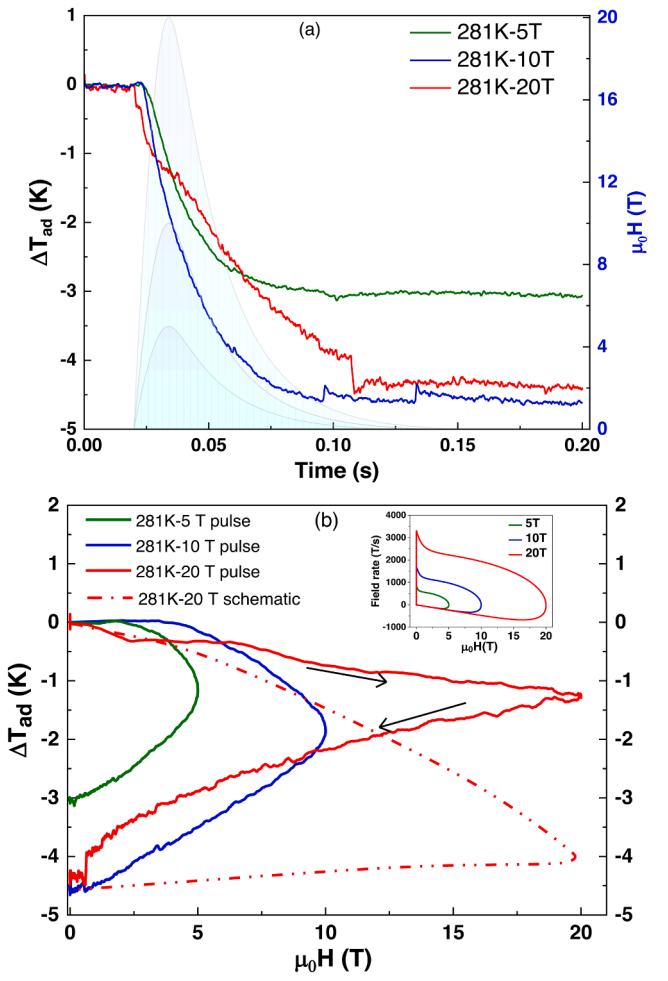


Fig. 10. (a) The ΔT_{ad} measurements of the ribbon at 281 K under pulsed magnetic fields of 5, 10, and 20 T. **(b)** Field dependence of ΔT_{ad} for the 5, 10 and 20 T pulses; the dash-dot line in Fig. 10 (b) schematically represents the continuation of the initial transformation-dominated trend that would be expected if the transformation could follow the magnetic-field variation without a pronounced kinetic delay and it is included only as a guide to the eye. The inset compares the field-sweep rates for 5, 10 and 20 T.

increasing the maximum field to 20 T does not produce additional net cooling. One possible explanation is that a field of approximately 10 T may already be sufficient to induce most of the field-driven martensite-to-austenite transformation accessible under the present experimental conditions. Consequently, a further increase in field does not necessarily result in a larger transformation-related ΔT_{ad}. However, since the martensite/austenite phase fractions were not measured directly during the pulsed-field experiment, a complete transformation at 10 T cannot be concluded.

Fig. 10 (b) further shows that the ΔT_{ad} *(H)* curves exhibit different slopes for the different pulse amplitudes, with the 20 T pulse showing the smallest slope. The higher-amplitude pulses are also associated with substantially higher field-sweep rates, reaching nearly 3000 T/s for the 20 T pulse. Therefore, non-equilibrium transformation dynamics may additionally influence the observed response. Since the maximum field and field-sweep rate are intrinsically coupled in the present pulsed-field measurements, their individual contributions cannot be quantitatively separated. Thus, the lack of additional cooling at 20 T may result from the combined influence of a limited additional field-induced transformation above 10 T, non-equilibrium transformation dynamics, and irreversible effects associated with the hysteretic transformation.

It should also be noted that, although the pulsed-field measurements

are approximately adiabatic, the strongly hysteretic first-order transformation is not necessarily isentropic. The fact that the sample returns to zero magnetic field at a temperature below its initial value indicates that the final thermodynamic state differs from the initial state, and that magnetic work associated with the irreversible transformation and hysteresis may contribute to the field-on/field-off process. Accordingly, the post-pulse cooling and its field dependence should not be interpreted solely in terms of a competition between inverse and conventional magnetocaloric contributions.

In this context, the dash-dot line in Fig. 10 (b) schematically represents the continuation of the initial transformation-dominated trend, assuming that the transformation could follow the magnetic-field variation without a pronounced kinetic delay. It is included only as a guide to the eye and should not be regarded as a quantitative prediction of the 20 T response. The deviation of the measured 20 T response from this schematic trend may reflect the combined influence of limited additional field-induced transformation and non-equilibrium transformation dynamics at the higher field-sweep rate. However, these effects cannot be independently separated in the present measurements.

As reported by Gottschall et al. [25], first-order magnetostructural transformations in Heusler alloys involve nucleation and phase-boundary motion, and the nucleation process can be sensitive to the magnetic-field sweep rate. However, in the present measurements, the effects of field amplitude, transformation extent, and field-sweep rate cannot be independently separated.

4. Conclusions

The present study demonstrates that the caloric response of melt-spun all- d-metal $Ni_{36}Co_{14}Mn_{37}Ti_{13}$ ribbons is strongly governed by the interplay between structural disorder, microstructural heterogeneity, and the first-order martensitic transformation. The ribbons predominantly crystallize in a disordered A2-like parent phase and exhibit a dual-grain microstructure, with small and large grains showing locally different transformation behavior. This grain-size distribution, together with the A2/B2-related structural disorder, contributes to the broadening of the transformation interval and is likely one of the main origins of the relatively large thermal hysteresis of approximately 34 K observed in the present ribbon.

Despite this broadened and hysteretic transformation, the ribbons exhibit a pronounced inverse magnetocaloric response near room temperature. More importantly, the direct pulsed-field ΔT_{ad} measurements reveal that the realistic caloric response cannot be described solely by the field-induced reverse martensitic transformation. Instead, the net cooling is governed by the combined influence of hysteresis, the extent of the field-induced transformation, and non-equilibrium transformation dynamics under different pulsed-field conditions. Remarkably, a 10 T pulse produces a larger net cooling than a 20 T pulse, highlighting the decisive role of kinetic and irreversible processes in determining the functional caloric response of first-order ribbon systems. Overall, the present results provide direct insight into the nonequilibrium caloric behavior of metamagnetic ribbon materials and demonstrate the importance of direct pulsed-field measurements for understanding realistic cooling performance under operating conditions.

CRediT authorship contribution statement

Ali Ghotbi Varzaneh: Writing – review & editing, Writing – original draft, Validation, Methodology, Investigation, Formal analysis, Data curation. **Mariana Ríos:** Writing – review & editing, Investigation, Formal analysis. **Catalina Salazar Mejía:** Writing – review & editing, Investigation, Formal analysis, Data curation, Conceptualization. **Meysam Norouzi-Inallu:** Writing – review & editing, Methodology, Investigation. **Gowtham Arivanandhan:** Writing – review & editing, Software, Investigation, Formal analysis. **Bagher Aslibeiki:** Writing – review & editing, Investigation, Formal analysis. **Tapati Sarkar:** Writing – review & editing, Investigation. **Manfred Kohl:** Writing – review & editing, Methodology, Conceptualization, Resources. **Tino Gottschall:** Writing – review & editing, Resources, Methodology, Investigation, Conceptualization. **Daniel Salazar:** Writing – review & editing, Investigation, Funding acquisition, Formal analysis, Conceptualization. **Jingyuan Xu:** Writing – review & editing, Supervision, Investigation, Funding acquisition.

Declaration of Competing Interest

The authors declare that they have no known competing financial interests or personal relationships that could have appeared to influence the work reported in this paper.

Acknowledgments

The authors gratefully acknowledge financial support from the Alexander von Humboldt Foundation and the Baden-Württemberg Stiftung. Financial support from the Basque Government Department of Education (projects KK-2025/00034 and IKUR-QT3), the project PID2022–138256NA-C22 funded by MCIN/AEI/10.13039/501100011033, and the European Space Agency through grant 4000148229/2025/NL/GLC (WISH Project) is also acknowledged. The authors further acknowledge the support of the Dresden High Magnetic Field Laboratory (HLD) at HZDR, a member of the European Magnetic Field Laboratory (EMFL). A.G. Varzaneh thanks Dr. Dmitry Busko for performing the XRD measurements. B. Aslibeiki and T. Sarkar gratefully acknowledge financial support from Stiftelsen Olle Engkvist Byggmästare (grant number 214–0346) and the Swedish Research Council (grant number 2021–03675).

References

[1] K.A. Gschneidner, Jr, V.K. Pecharsky, A. Tsokol, "Recent developments in magnetocaloric materials, Rep. Progress. Phys. 68 (6) (2005) 1479–1539.
[2] T. Gottschall, K.P. Skokov, D. Benke, M.E. Gruner, O. Gutfleisch, "Contradictory role of the magnetic contribution in inverse magnetocaloric Heusler materials, Phys. Rev. B 93 (18) (2016) 184431.
[3] L. Pfeuffer, et al., "Influence of microstructure on the application of Ni-Mn-In Heusler compounds for multicaloric cooling using magnetic field and uniaxial stress, Acta Mater. 217 (2021) 117157.
[4] J. Liu, T. Gottschall, K.P. Skokov, J.D. Moore, O. Gutfleisch, "Giant magnetocaloric effect driven by structural transitions, Nat. Mater. 11 (7) (2012) 620–626.
[5] Z. Wei, et al., "Realization of multifunctional shape-memory ferromagnets in all-d-metal Heusler phases, Appl. Phys. Lett. 107 (2) (2015).
[6] A. Taubel, et al., "Tailoring magnetocaloric effect in all-d-metal Ni-Co-Mn-Ti Heusler alloys: a combined experimental and theoretical study, Acta Mater. 201 (2020) 425–434.
[7] Z. Guan, et al., "Large magnetocaloric effect and excellent mechanical properties near room temperature in Ni-Co-Mn-Ti non-textured polycrystalline alloys, Appl. Phys. Lett. 119 (5) (2021).
[8] B. Beckmann, et al., "Giant magnetocaloric effect of Ni-Co-Mn-Ti all-d Heusler alloys in high magnetic fields, Acta Mater. 282 (2025) 120460.
[9] Z. Guan, et al., "Realizing overall trade-off of giant caloric effect, wide working temperature range and ultrahigh cyclic stability in Ni-Co-Mn-Ti-B multiferroic phase transformation alloy, Mater. Today Phys. (2025) 102001.
[10] H. Tang, Z. Guan, Y. Wu, Z. Li, J. Liu, X. Lu, "Boosting caloric performances of Ni-Co-Mn-Ti shape memory alloy for multi-scenario refrigeration by spark plasma sintering, Materials 18 (20) (2025) 4691.
[11] K. Qiao, et al., "Direct observation of microstructure effect on martensitic transformation in multifunctional Ni–Co–Mn–Ti alloy, Small Struct. 7 (1) (2026) e202500623.
[12] H. Wang, et al., "Enhanced cyclability of elastocaloric effect in a directionally solidified $Ni_{37.5}Co_{12.5}Mn_{34}Ti_{16}$ alloy by introducing η-Ni3Ti precipitates, Acta Mater. (2025) 121693.
[13] H.N. Bez, et al., "Giant enhancement of the magnetocaloric response in Ni–Co–Mn–Ti by rapid solidification, Acta Mater. 173 (2019) 225–230.
[14] C. Ma, K. Liu, X. Han, S. Yang, N. Ye, J. Tang, "Martensitic transformation and magnetocaloric effect in melt-spun $Mn_{50}Ni_{31.5}Co_{8.5}Ti_{10}$ all-3d-metal alloy ribbons, J. Magn. Magn. Mater. 493 (2020) 165733.
[15] K. Liu, et al., "Martensitic transformation and giant magneto-functional properties in all-d-metal Ni-Co-Mn-Ti alloy ribbons, J. Alloy. Compd. 790 (2019) 78–92.
[16] M. López-Cruz, R. Varga, J.L. Sánchez Llamazares, "Magnetostructural transformation and magnetocaloric properties of $(Ni_{37.5}Co_{12.5}Mn_{35}Ti_{15})_{100-x}B_x$ (x= 0.0 and 0.4) melt-spun ribbons, Metals 14 (2) (2024) 216.

[17] K. Liu, et al., "Magnetic-field-induced metamagnetic reverse martensitic transformation and magnetocaloric effect in all-d-metal $Ni_{36.0}Co_{14.0}Mn_{35.7}Ti_{14.3}$ alloy ribbons, Intermetallics 110 (2019) 106472.
[18] S. Ma, et al., "Wheel speed-dependent martensitic transformation and magnetocaloric effect in Ni–Co–Mn–Sn ferromagnetic shape memory alloy ribbons, Acta Mater. 90 (2015) 292–302.
[19] A.G. Varzaneh, et al., "Tailoring Ni–Co–Mn–Sn ribbons by Ge doping for enhanced magnetocaloric effect, Adv. Electron. Mater. 11 (20) (2025) e00596.
[20] M. López-Cruz, J. Zamora, J.S. Llamazares, "Spark plasma sintering consolidation of all-d-metal Ni-Co-Mn-Ti alloys from melt-spun ribbons: magnetostructural and magnetocaloric characterization,", J. Magn. Magn. Mater. (2025) 173761.
[21] A. Kamantsev, et al., "Magnetic properties of melt-spun ribbons of heusler $Ni_{37}Co_{13}Mn_{35}Ti_{15}$ alloy under external pressure, Phys. Met. Metallogr. 126 (9) (2025) 1043–1050.
[22] S. Mandal, T.K. Nath, "Non-itinerant-type ferromagnetism and the magnetocaloric response of quinary all-d-metal ribbon: $Ni_{35}Mn_{34.5}Co_{14}Fe_1Ti_{15.5}$, J. Phys. D Appl. Phys. 57 (49) (2024) 495304.
[23] M. López-Cruz, J. Zamora, C.F. Sánchez-Valdés, J.L. Sánchez Llamazares, "On the synthesis, structural transformation and magnetocaloric behavior of $Ni_{37.5}Co_{12.5}Mn_{35}Ti_{15}$ melt-spun ribbons, AIP Adv. 11 (1) (2021).
[24] F. Zhang, I. Batashev, N. Van Dijk, E. Brück, "Reduced hysteresis and enhanced giant magnetocaloric effect in B-doped all-d-metal Ni-Co-Mn-Ti-based Heusler materials,", Phys. Rev. Appl. 17 (5) (2022) 054032.
[25] T. Gottschall, et al., "Dynamical effects of the martensitic transition in magnetocaloric heusler alloys from direct Δ T ad measurements under different magnetic-field-sweep rates, Phys. Rev. Appl. 5 (2) (2016) 024013.
[26] C. Salazar Mejía, et al., "On the high-field characterization of magnetocaloric materials using pulsed magnetic fields, J. Phys. Energy 5 (3) (2023) 034006.
[27] B. Beckmann, et al., "Dissipation losses limiting first-order phase transition materials in cryogenic caloric cooling: a case study on all-d-metal Ni (-Co)-Mn-Ti Heusler alloys, Acta Mater. 246 (2023) 118695.
[28] O. Gutfleisch, et al., "Mastering hysteresis in magnetocaloric materials, Philos. Trans. R. Soc. A Math. Phys. Eng. Sci. 374 (2074) (2016) 20150308.
[29] T. Gottschall, et al., "A multicaloric cooling cycle that exploits thermal hysteresis, Nat. Mater. 17 (10) (2018) 929–934.
[30] A. Kamantsev, et al., "Giant irreversibility of the inverse magnetocaloric effect in the $Ni_{47}Mn_{40}Sn_{12.5}Cu_{0.5}$ Heusler alloy, Appl. Phys. Lett. 123 (20) (2023).
[31] Z. Li, et al., "Giant low-field magnetocaloric effect in Si alloyed Ni-Co-Mn-In alloys, Scr. Mater. 159 (2019) 113–118.
[32] D. Salas, et al., "Effects of composition and crystallographic ordering on the ferromagnetic transition in NiCoMnIn magnetic shape memory alloys, Acta Mater. 166 (2019) 630–637.
[33] M. Şaşmaz, F. Dreist, I. Iglesias, A. Çakır, M. Farle, M. Acet, "Decomposition in Ni-Co-Mn-In functional Heusler alloys and its effect on shell-ferromagnetic and magnetocaloric effects,", Phys. Rev. B 102 (6) (2020) 064401.
[34] D. Koch, et al., "Chemical long range ordering in all-d-metal Heusler alloys, J. Appl. Phys. 131 (7) (2022).
[35] S. Sun, et al., "Extraordinary mechanical properties and room-temperature magnetocaloric effects in spark plasma sintered all-d-metal Ni-Co-Mn-Ti alloy, J. Alloy. Compd. 976 (2024) 173406.
[36] S. Venkatesan, et al., "Realization of enhanced refrigeration capacity with non-hysteretic behavior in $Ni_{40}Gd_5Co_cMn_{37}In_{12}Si_1$ alloy near room temperature at 2T, ACS Appl. Energy Mater. 5 (12) (2022) 15959–15971.
[37] S. Ghosh, et al., "Room temperature giant magneto-caloric effect in $Ni_{45}Mn_{44}Sn_{11-x}In_x$ (x= 1, 3) disordered Heusler alloy: the role of martensite transition, J. Magn. Magn. Mater. 562 (2022) 169797.
[38] A. Taubel, et al., "A comparative study on the magnetocaloric properties of Ni-Mn-X (-Co) Heusler Alloys, Phys. Status Solidi (b) 255 (2) (2018) 1700331.
[39] H. Sepehri-Amin, A. Taubel, T. Ohkubo, K. Skokov, O. Gutfleisch, K. Hono, "Microstructural origin of hysteresis in Ni-Mn-In based magnetocaloric compounds, Acta Mater. 147 (2018) 342–349.
[40] A.M.G. Carvalho, A. Coelho, P. Von Ranke, C. Alves, "The isothermal variation of the entropy (ΔS_T) may be miscalculated from magnetization isotherms in some cases: MnAs and $Gd_5Ge_2Si_2$ compounds as examples, J. Alloy. Compd. 509 (8) (2011) 3452–3456.
[41] M.N. Inallu, et al., "Magnetocaloric effect in W-doped Ni–Mn–Sn alloy probed by direct and indirect measurements, J. Phys. D Appl. Phys. 52 (23) (2019) 235001.
[42] A.G. Varzaneh, et al., "Magnetic and magnetocaloric properties of $Ni_{47}Mn_{40}Sn_{13-x}Zn_x$ alloys: Direct measurements and first-principles calculations, Phys. Rev. B 101 (13) (2020) 134403.
[43] P. Lázpita, A. Pérez-Checa, J.M. Barandiarán, E.L. Ammerlaan, U. Zeitler, V. Chernenko, "Suppression of martensitic transformation in Ni-Mn-In metamagnetic shape memory alloy under very strong magnetic field,", J. Alloy. Compd. 874 (2021) 159814.
[44] L. Griffith, Y. Mudryk, J. Slaughter, V. Pecharsky, "Material-based figure of merit for caloric materials, J. Appl. Phys. 123 (3) (2018).
[45] T. Gottschall, et al., "Making a cool choice: the materials library of magnetic refrigeration, Adv. Energy Mater. 9 (34) (2019) 1901322.
[46] A.N. Khan, et al., "Enhanced local homogeneity obtained by induction melting for optimizing reversible magnetocaloric response in All-d-metal Ni (Co)-Mn-Ti Heusler alloys, J. Alloy. Compd. (2026) 186135.
[47] A.N. Khan, L.M. Moreno-Ramírez, Á. Díaz-García, J.Y. Law, V. Franco, "All-d-metal Ni (Co)-Mn (X)-Ti (X= Fe or Cr) Heusler alloys: enhanced magnetocaloric effect for moderate magnetic fields,", J. Alloy. Compd. 931 (2023) 167559.
[48] S. Samanta, S. Ghosh, S. Chatterjee, K. Mandal, "Large magnetocaloric effect and magnetoresistance in Fe-Co doped Ni50-x (FeCo) xMn37Ti13 all-d-metal Heusler alloys, J. Alloy. Compd. 910 (2022) 164929.
[49] Y. Li, Y. Pan, "The second-order magnetic transformation and magnetocaloric effect in all-d-metal Heusler ribbon $Ni_{35}Co_{15}Mn_{34}Ti_{16}$, Mater. Lett. 376 (2024) 137281.